



SPAGINS: semiempirical parameterization for fragments in gamma-induced nuclear spallation

Hui-Ling Wei¹ · Meng-Die Zhou^{1,2} · Pu Jiao^{1,2} · Yu-Ting Wang¹ · Jie Pu¹ · Kai-Xuan Cheng¹ · Ya-Fei Guo¹ · Chun-Yuan Qiao¹ · Gong-Tao Fan² · Hong-Wei Wang² · Chun-Wang Ma^{1,3}

Received: 18 July 2023 / Revised: 11 October 2023 / Accepted: 13 October 2023 / Published online: 2 December 2023

© The Author(s), under exclusive licence to China Science Publishing & Media Ltd. (Science Press), Shanghai Institute of Applied Physics, the Chinese Academy of Sciences, Chinese Nuclear Society 2023

Abstract

From the empirical phenomena of fragment distributions in nuclear spallation reactions, semiempirical formulas named SPAGINS were constructed to predict fragment cross-sections in high-energy γ -induced nuclear spallation reactions (PNSR). In constructing the SPAGINS formulas, theoretical models, including the TALYS toolkit, SPACS, and Rudstam formulas, were employed to study the general phenomenon of fragment distributions in PNSR with incident energies ranging from 100 to 1000 MeV. Considering the primary characteristics of PNSR, the SPAGINS formulas modify the EPAX and SPACS formulas and efficiently reproduce the measured data. The SPAGINS formulas provide a new and effective tool for predicting fragment production in PNSR.

Keywords High-energy gamma-rays · Spallation reaction · Fragment cross-section · Empirical formula · EPAX · SPACS · TALYS

1 Introduction

The nuclear spallation reaction is a violent reaction induced by light-charged particles (LCPs), such as p , d , t , ^3He , α , and uncharged particles, such as neutrons and high-energy γ . In nuclear spallation reactions, various residual fragments are produced. Fragment production cross-sections in spallation reactions are important because they provide considerable information about the evolving reaction system [1–3]. γ -induced nuclear reactions, called photonuclear reactions (PNRs), have been extensively studied in recent decades [4]. Because only electromagnetic interaction occurs between

photons and nuclei [5–7], PNRs provide a unique tool for studying the properties of nuclear forces [8], nuclear structural parameters, nuclear astrophysics, and other fields [9–11]. The past few decades have witnessed a renaissance of experimental PNRs in laboratories, partly because of the emergence of new accelerator-based gamma sources that create quasi-monoenergetic photon spectra with high credibility based on laser Compton backscattering (LCB) [12]. The concept of producing high-energy photons from light photons colliding with extremely relativistic electrons was proposed by Milburn [13] and Arutyunian et al. [14]. Bemporad et al. used a ruby laser scattered with 6-GeV electrons to produce 425 MeV γ photons 2 years later [15]. In 2013, the LEPS-II (the laser electron–photon experiment at SPring-8) produced 1.4–2.4 or 1.4–2.9 GeV γ beamlines. With the development of SLEGS (Shanghai Laser Electron Gamma Source) at the SSRF (Shanghai Synchrotron Radiation Facility) [16, 17] and completion of the future SHINE (Shanghai High repetition rate XFEL aNd Extreme light facility) construction [18, 19], the gamma energy of Compton-scattered light sources based on LINAC (LINear ACcelerator) will be on the order of GeV. An area of γ energy larger than 140 MeV is mainly related to the fields of hadron physics, where mesons can be produced [20, 21]. GeV

This work was supported by the Program for Innovative Research Team (in Science and Technology) in University of Henan Province (No. 21IRTSTHN011), China.

✉ Chun-Wang Ma
machunwang@126.com; machw@htu.edu.cn

¹ Institute of Particle and Nuclear Physics, College of Physics, Henan Normal University, Xixiang 453007, China

² Shanghai Advanced Research Institute, Chinese Academy of Sciences, Shanghai 201204, China

³ Institute of Nuclear Science and Technology, Henan Academy of Science, Zhengzhou 450046, China

photon beamline can be used to investigate subatomic and nuclear physics.

High-energy γ -rays can induce nuclear spallation reactions, which are called photonuclear spallation reactions (PNSR). In recent years, considerable research has been conducted on the photonuclear spallation of heavy nuclei [22–24]. In 1986, the experimental study of PNSR by Shibata et al. [4] included the measurement of the cross-sections of 24 nuclides in the $\gamma + {}^{\text{nat}}\text{Cu}$ reaction. The γ -rays were made from bremsstrahlung with maximum end-point energies from 100 MeV to 1 GeV by counting the irradiated targets, assuming a $1/E$ dependence of the bremsstrahlung spectrum and giving a cross-section with a unit of mb [milli-barn/equivalent quantum], and the data were used to monitor the flux of bremsstrahlung quanta. The cross-sections of the fragments produced in nuclear spallation shared similar characteristics, although they were induced by different incident particles. Jonsson et al. compared the fragment yields in γ and LCPs-induced nuclear spallation reactions, and some photon-induced spallation cross-sections in ${}^{127}\text{I}$ were also estimated. They conducted experiments on γ -induced nuclear reactions above 1 GeV and discussed the principles of high-energy reactions [25–27].

The mechanism of spallation reactions was treated as a two-step cascade-evaporation process according to Serber et al., in which the first step describes the cascade process and the second describes the evaporation process [27–29]. In the cascade process, the incoming projectile initiates a chain cascade by interacting with nucleons inside the target nucleus, where numerous particles are ejected from the nucleus, and residual target nuclei form highly excited hot fragments. Then, in the evaporation stage, hot fragments are deexcited by evaporating nucleons or nuclear clusters to form the final products. However, in the evaporation process, the memory of cascade residual formation is lost, which leads to a very similar deexcitation process between the photon- and proton-induced reactions [30–32].

The main improvement in fragment production in PNRs was the development of the TALYS toolkit [33]. The TALYS toolkit provides a complete and accurate simulation of the nuclear reactions of light incident particles with energies up to 200 MeV using an optical reaction model. However, a notable difference was found between the experimental and TALYS predicted fragment cross-sections [34]. The cascade-evaporation model shows that the fragment cross-sections in PNSR and proton-induced spallation reactions share similarities [29, 35, 36], which motivated us to compare their fragment distributions. Considering the lack of systematic prediction models for fragment cross-sections in PNSR, we propose a semiempirical parameterization for fragments in gamma-induced nuclear spallation (SPAGINS) based on available measured data, as well as theoretical guidance from the EPAX, SPACS, and TALYS models.

The remainder of this paper is organized as follows. In Sect. 2, a brief introduction to the SPAGINS formalism is provided. In Sect. 3, the construction process of SPAGINS formulas and predicted results by SPAGINS formalism are compared to Rudstam fitting data and TALYS predictions, as well as the measured data. A summary of the study is provided in Sect. 4.

2 Methods

2.1 TALYS toolkit

The latest version, TALYS-1.96 [33, 37], was adopted in this study to guide the construction and verification of SPAGINS formulas. The optical reaction model governs the basic concepts in the TALYS toolkit [38]. TALYS toolkit includes nuclear reactions induced by n , p , d , t , ${}^3\text{He}$, α , γ , and with incident energies ranging from 1 keV to approximately 200 MeV [39]. The valid range of target nuclei was between 12 and 339 ($12 < A < 339$). In TALYS, the nuclear reaction process is divided into three stages: (1) the independent particle stage, in which the incident particle is partially scattered and partially absorbed, similar to light waves passing through a translucent glass sphere; (2) the compound system stage, which follows the time of the incident particle being absorbed by the target nucleus, energy exchange occurs between them, and a compound system is formed; and (3) the end stage, in which the compound system is decomposed into outgoing particles and residual fragments. The calculation of the cross-section of a specific residual fragment is based on the manual of the TALYS toolkit [40]. The default input parameters were adopted in TALYS calculations.

2.2 Empirical EPAX and SPACS formulas

The cross-sections of the fragment productions with the mass number A and charge number Z for spallation reactions can be divided into three terms: the total reaction cross-section, mass yield distribution, and charge distribution, which were first proposed by Rudstam [41, 42], the five-parameter fitting formula, and the development of empirical EPAX and SPACS formulas. The five parameters in the five-parameter fitting formula (named the Rudstam formula in this article) were obtained by fitting with the nonlinear least-squares method; thus, it cannot be used to predict nuclides.

The main characteristics of fragment production in spallation reactions were included in the EPAX parameterization (a universal empirical parameterization of fragmentation cross-sections), which was proposed by Sümmerer et al. in 1990. The EPAX formulas inherit the ideas of Rudstam and Silberberg [43], who aimed to describe the fragmentation of medium-to-heavy mass projectiles. The fragment

cross-section was independent of the incident energy of the reaction system above 140 MeV/u. The updated versions of EPAX2 and EPAX3 successfully describe the production of fragments in projectile fragmentation reactions above 100 MeV/u [44, 45]. The improved formulas for fragments produced in nuclear spallation reactions based on EPAX have been proposed by Schmitt et al. in 2014, which is named SPACS (a semiempirical parameterization for isotopic spallation cross-sections) [46, 47]. In the SPACS formulas, more than 40 parameters were adopted to reestablish the mass yield and explicitly state the dependence of the yields of the residual fragments on the bombardment energy [48]. The charge distribution of the fragments was given by EPAX [44, 45, 49]. The dependence of the fragment cross-section on the collision energy, shell structure, and even-odd effect was further considered in the SPACS formulas. The readers can refer to Refs. [44, 45] for detailed descriptions of fragments cross-sections in EPAX and to Ref. [47] for SPACS parameterizations. The main formulas in both EPAX and SPACS were adopted to construct the SPAGINS formulas in this study, which are introduced in Sect. 2.3.

2.3 Phenomenological isotopic distributions in PNSR

In this subsection, the fragment isotopic cross-sectional distributions are compared to determine the basic ideas for developing the SPAGINS formulas. In the first step, we illustrated the similarity in fragment production between γ and proton-induced nuclear spallation reactions. The TALYS-1.96 was adopted to predict the isotopic distributions for the $\gamma+^{63}\text{Cu}$ and $p+^{62}\text{Ni}$ reactions at 100 and 200 MeV, where the mass and charge numbers of the reaction systems were the same. In Fig. 1a and b, the isotopic cross-section distributions in the $\gamma+^{63}\text{Cu}$ reaction (open symbols) share the same pattern as those in the $p+^{62}\text{Ni}$ reaction except that they have smaller magnitudes. The quantity is defined as the ratio

of the fragment cross-section in proton-induced spallation ($\sigma(f)_p$) to γ induces spallation ($\sigma(f)_\gamma$), $R_{p/\gamma} \equiv \sigma(f)_p/\sigma(f)_\gamma$. The $R_{p/\gamma}$ values for the isotopic cross-sections in $p+^{62}\text{Ni}$ and $\gamma+^{63}\text{Cu}$ reactions are shown in Fig. 1a and b, respectively. The $R_{p/\gamma}$ values for isotopes in the reactions at an incident energy of 100 MeV were approximately 150 and 400 at an incident energy of 200 MeV. This indicates that the formula for fragment cross-sections in the proton-induced nuclear spallation reaction can be adopted for γ -induced ones by further considering the incident energy dependence.

2.4 Rudstam formula

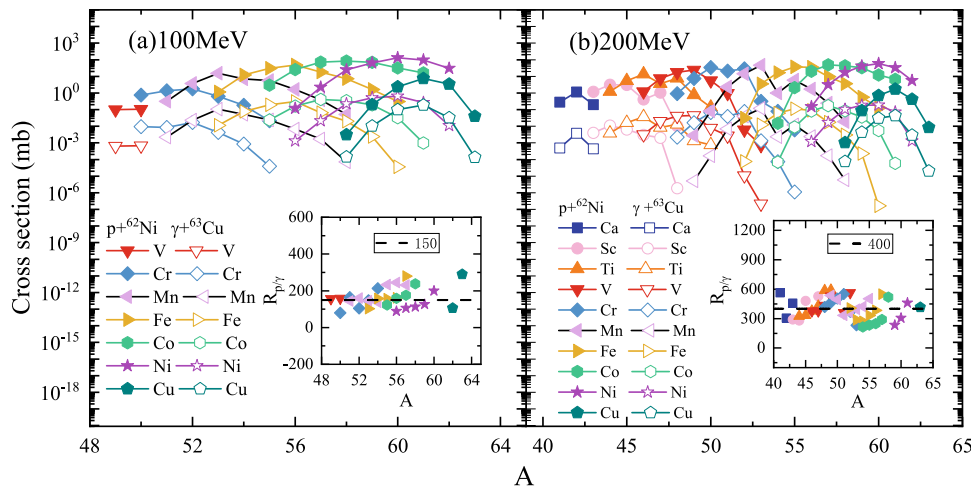
The Rudstam formula has two types of distributions for determining the fragment cross-section in PNSR. One uses charge distribution and mass yield distribution (CDMD), and the other uses isotopic distribution and elemental distribution (IDED) [41]. In this study, the CDMD in Ref. [4] is adopted, and the Rudstam formula reads,

$$\sigma(Z, A) = \frac{\hat{\sigma}PW^{2/3}}{1.79(e^{PA_t} - 1)} \exp(PA - W|Z - SA + TA^2|^{3/2}), \tag{1}$$

where $P, W, S, T,$ and $\hat{\sigma}$ are free parameters. P defines the slope of the mass yield curve, and W defines the charge distribution width. S and T describe the most probable charge and define the peak locations of the charge distribution (or isotopic distribution), respectively. $\hat{\sigma}$ denotes the total inelastic yield of the reaction. The parameters were determined by performing a nonlinear least-squares fit to the measured fragments in $\gamma+^{nat}\text{Cu}$ PNSR within the range of E_γ from 100 to 1000 MeV [4] and adopted in this study to investigate the incident energy dependence of the fragment cross-section (see Sect. 3.1).

In the second step, with the help of the Rudstam formula, the fragment cross-sections of chromium isotopes

Fig. 1 (Color online) The calculated isotopic cross-section for fragments by TALYS-1.96 in the $\gamma+^{63}\text{Cu}$ and $p+^{62}\text{Ni}$ reactions at $E_\gamma = 100$ MeV [in (a)] and 200 MeV [in (b)], respectively. The ratio of the isotopic cross-sections in the $p+^{62}\text{Ni}$ and $\gamma+^{63}\text{Cu}$ reactions is plotted in the inserted figure



were compared for the $\gamma+^{64}\text{Cu}$ reaction at incident energies ranging from $E_\gamma = 100$ to 1000 MeV.

3 SPAGINS formulas

In this section, the procedure for developing the SPAGINS formulas is first described, and then, the SPAGINS predictions are verified to fragment the cross-sections in PNSR through a comparison with the measured results.

3.1 Developing SPAGINS formulas

For a residual fragment (Z, A) produced in fragmentation or spallation reactions, the cross-section can be described as follows:

$$\sigma(A, Z) = \sigma_R Y(A) Y(Z_{\text{prob}} - Z)|_A, \quad (2)$$

where σ_R is the normalized total reaction cross-section [50, 51], and $Y(A)$ is the mass yield. The third term represents the isobaric yield for a given mass A . The construction of SPAGINS formulas started with this formula to describe fragment production. In this study, modifications were made to the mass and charge distribution terms.

The terms that influence σ_R are the masses of the projectile A_{proj} and target A_{tar} . The energy-dependent function δ_E considers the effects of transparency, Pauli blocking, and the Coulomb barrier B . The energy of the collision system is in the center-of-mass framework, and the quantity χ_m corrects the intensity of the optical model interaction at low energies [46, 47]. Because photonuclear reactions involve only electromagnetic interactions, the Coulomb barrier is zero. The mathematical expressions for these quantities are given in the SPACS formalism [5, 6].

The measured fragment cross-sections in the $\gamma+\text{Cu}$ spallation reaction [4] were used as an example to perform the analysis. Natural copper has two stable isotopes: 69.17% ^{63}Cu and 30.83% ^{65}Cu . The findings of this study revealed that the isotopic effects in the fragment cross-sections were minimal. Thus, ^{64}Cu was adopted as the spallation target instead of natural copper, which is mainly composed of ^{63}Cu and ^{65}Cu . To maintain the same masses and charge numbers in spallation systems, a proton-induced system of $p+^{63}\text{Ni}$ was selected for comparison.

The calculated fragment cross-sections were compared to the measured cross-sections according to two main aspects. The first method considers the incident energy dependence of the fragments. With an increase in energy, the cross-sections of the residual fragments produced by PNSR increase exponentially. The second factor is the charge number Z . For the generation of different types of residual fragments, the

difference between the calculated residual fragment cross-section and experimental value constantly changes with the change in charge number. To reduce the difference between the section value calculated using the empirical formula and the experimental value, the corrections for energy and charge are necessary.

Schmitt et al. found that the mass distributions of the spallation and fragmentation reactions cannot be described by the same mathematical expression [46]. Importantly, in spallation reactions, the energy dependence of $Y(A)$ cannot be ignored [44, 45, 48]. Schmitt et al. added an energy dependence related to $Y(A)$ to the SPACS formalism [43, 45, 49]. The energy dependence of $Y(A)$ is discussed in Sect. 3.2.

The third term in Eq. (2), $Y(Z_{\text{prob}} - Z)|_A$, describes the isotopic distribution, which is insensitive to the interaction mechanism but is mainly controlled by the level density. In this study, the application ranges for certain quantities were modified. The magnitude of the brute force factor was changed, and the charge dependence was modified, as shown in Sect. 3.2.

3.2 Main formulas in SPAGINS

Mass yield $Y(A)$ in Eq. (2) is divided into two parts considering the fragment contributions of the central collisions $Y(A)_{\text{cent}}$ and peripheral collisions $Y(A)_{\text{prph}}$, which are expressed as follows:

$$Y(A) = Y(A)_{\text{cent}} + Y(A)_{\text{prph}}. \quad (3)$$

$Y(A)$ depends exponentially on the incident energy. Particularly, the production of Cr isotopes was studied to determine their dependence on the incident energy. To observe how the fragment cross-section depends on E_γ , the Rudstam formula in Eq. (1) with the parameters according to Ref. [4] is

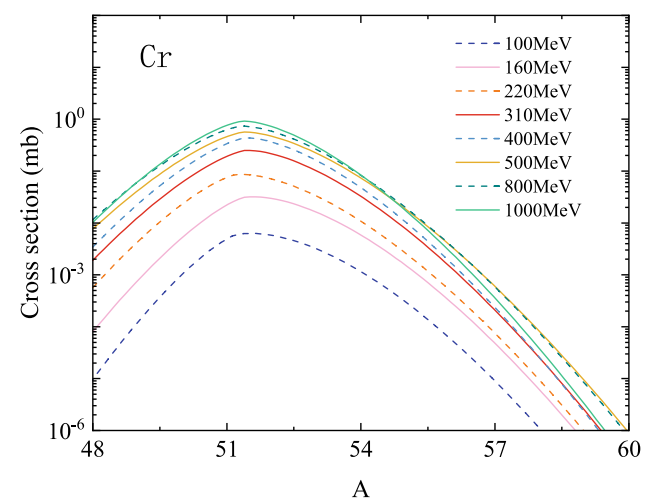


Fig. 2 (Color online) The Rudstam fitting formula according to Eq. (1) for production cross-sections of Cr isotopes in $\gamma+^{64}\text{Cu}$ reactions from 100 to 1000 MeV

adopted to estimate the Cr isotopic productions in $\gamma+^{64}\text{Cu}$ reactions with E_γ from 100 MeV to 1 GeV (see Fig. 2). Within the range of $100 \text{ MeV} \leq E_\gamma \leq 500 \text{ MeV}$, the isotopic distribution increases with the incident energy, whereas it becomes very similar when $E_\gamma > 500 \text{ MeV}$. Thus, the trend of $Y(A)$ is parameterized as the following equations for different incident energy ranges:

$$Y'(A) = G \cdot Y(A). \tag{4}$$

G depends on the incident energy in the form of

$$G = \begin{cases} 10^{(E_\gamma-100)/100}, & 100 \leq E_\gamma < 220; \\ 10^{(E_\gamma-220)/300}, & 220 \leq E_\gamma < 500; \\ 10^{(E_\gamma-500)/2000}, & 500 \leq E_\gamma \leq 1000. \end{cases} \tag{5}$$

E_γ is sorted into three different ranges: (1) from 100 to 220 MeV, (2) from 220 to 500 MeV, and (3) from 500 to 1000 MeV, which empirically reflect the energy dependence of the isotopic distributions shown in Fig. 2.

In the EPAX formulas, Z_{prob} describes the deviation of the most probable charge from the position of β -stability valley (Z_β) by the quantity Δ . For photonuclear spallation reaction, the parameters Δ used in EPAX are as follows:

$$\Delta = \Delta_5 A^2, \tag{6}$$

$$\Delta' = \Delta[1 + d_1(A/A_{\text{proj}} - d_2)^2]. \tag{7}$$

The SPACS formula modifies the parameter R in EPAX, which is also the formula used:

$$R = R_0^{\text{n,p}} \cdot R^{\text{phy}} \\ R_0^{\text{n,p}} = r_0 \exp[r_4(Z_{\text{proj}} - Z_{\beta\text{p}})], \tag{8} \\ R^{\text{phy}} = \exp\{-\ln[R_1(A/t_2)]\}.$$

The residual fragments in the spallation reaction can be divided into proton- and neutron-rich fragments, which are parameterized in different forms. The SPACS refined the normalization of the charge-dispersion curve based on EPAX3, and the so-called ‘‘brute force factor’’ f_n (f_p) is used to adjust the distribution of neutron-rich (proton-rich) fragments. For $(Z_\beta - Z) > (Z_{\text{proj}} - Z_{\beta\text{p}} + b_2)$,

$$f_n = 10^{[-b_1|Z_{\text{proj}}-Z_{\beta\text{p}}|(Z_\beta-Z+Z_{\text{proj}}-Z_{\beta\text{p}}+b_2)^3]}. \tag{9}$$

Otherwise, $f_n = 1$. For $Z > Z_{\text{exp}}$

$$f_p = 1/[10^{dF/dZ}]^{(Z-Z_{\text{exp}})}. \tag{10}$$

When the charge of the residual fragment was less than that of the target nucleus, the SPACS predictions agreed with the measured data, whereas when the charge of the residual fragment was close to that of the target nucleus, the SPACS predictions differed significantly from the measured values. In addition, f_n and f_p determine the peak position of the Gaussian distribution of the isotopes. The following conditions of ‘‘brute force factors’’ are formulated for those residual fragments on the valley of β stability. When $Z_\beta > Z - 0.75$, f_n is used, and f_p is used in all other cases. For these reasons, in $\gamma+^{64}\text{Cu}$ spallation reactions, the residual fragments with charge numbers ranging from 21 to 29 are divided into three groups. The first group consisted of residual fragments with $Z < 21$, the second group consisted of those with $21 < Z < 26$, and the last group consisted of those with $Z > 26$. The parameterized brute force factor is described in Sect. 6.

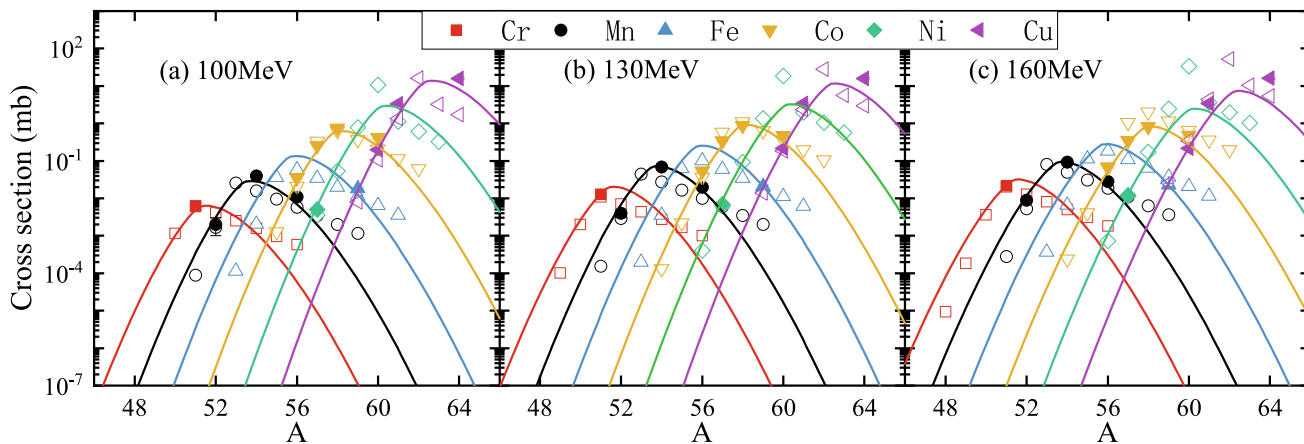


Fig. 3 (Color online) The isotopic cross-section in the 100 MeV (a), 130 MeV (b), and 160 MeV (c) $\gamma+^{64}\text{Cu}$ reactions. The SPAGINS predictions are plotted as open symbols, and full lines represent the

fitting lines by the Rudstam formula, which are used to guide the eye. The measured fragments in the $\gamma+^{\text{nat}}\text{Cu}$ reactions (taken from Ref. [4]) are plotted in full symbols

3.3 Validation for SPAGINS formulas

In Fig. 3, the predicted isotopic cross-section distributions by the SPAGINS formulas in $\gamma+^{64}\text{Cu}$ reactions and solid line used to guide the eye are the five-parameter fitting formula from Rudstam. The cross-sections for fragments in the corresponding $\gamma+^{\text{nat}}\text{Cu}$ results are plotted for comparison in solid symbols, for which the incident energies E_γ range from 100 MeV to 1 GeV at 100, 130, 160, 220, 310, 400, 500, 800, and 1000 MeV. The mass (charge) number of the fragments ranged from 38 (19) to 64 (29). Owing to the similarities in the types of graphs, only E_γ values at 100, 130, and 160 are displayed in this study. The SPAGINS formula reproduced the measured data well, except for those near the target isotopes.

The excitation function of the residual fragment, that is, the dependence of the fragment cross-section on the incident energy of the reaction, reflects how the probability changes with E_γ . Figure 4 shows the cross-sections of fragments

from ^{42}K to ^{61}Cu , which are produced in the $\gamma+^{64}\text{Cu}$ reaction within E_γ from 100 MeV to 1 GeV, in which both the SPAGINS predictions and Rudstam fitting data are compared to the measured results of the $\gamma+^{\text{nat}}\text{Cu}$ reaction. Both the SPAGINS and Rudstam formulas can reproduce the experimental excitation functions in $\gamma+^{\text{nat}}\text{Cu}$ reactions, except that the SPAGINS prediction underestimates the measured function for ^{57}Ni . In the SPAGINS formula, Eq. (26) in the APPENDIX, and the brute force factors f_n and f_p , the fitting data of the Rudstam formula depends on E_γ and influence the fragment cross-section [46] when E_γ is changed. In the Rudstam formula, all five parameters depend on incident energy [41]. The good agreement between the SPAGINS predictions and measured results for the excitation curves of fragments suggests that the parameterization of the incident energy dependence of fragment cross-sections reflects the inner mechanism of fragment production in PNSR. The mean relative errors are shown in Fig. 5. The dashed line indicates that $\sigma_{\text{exp}}/\sigma_{\text{cal}}$ is equal to 1.

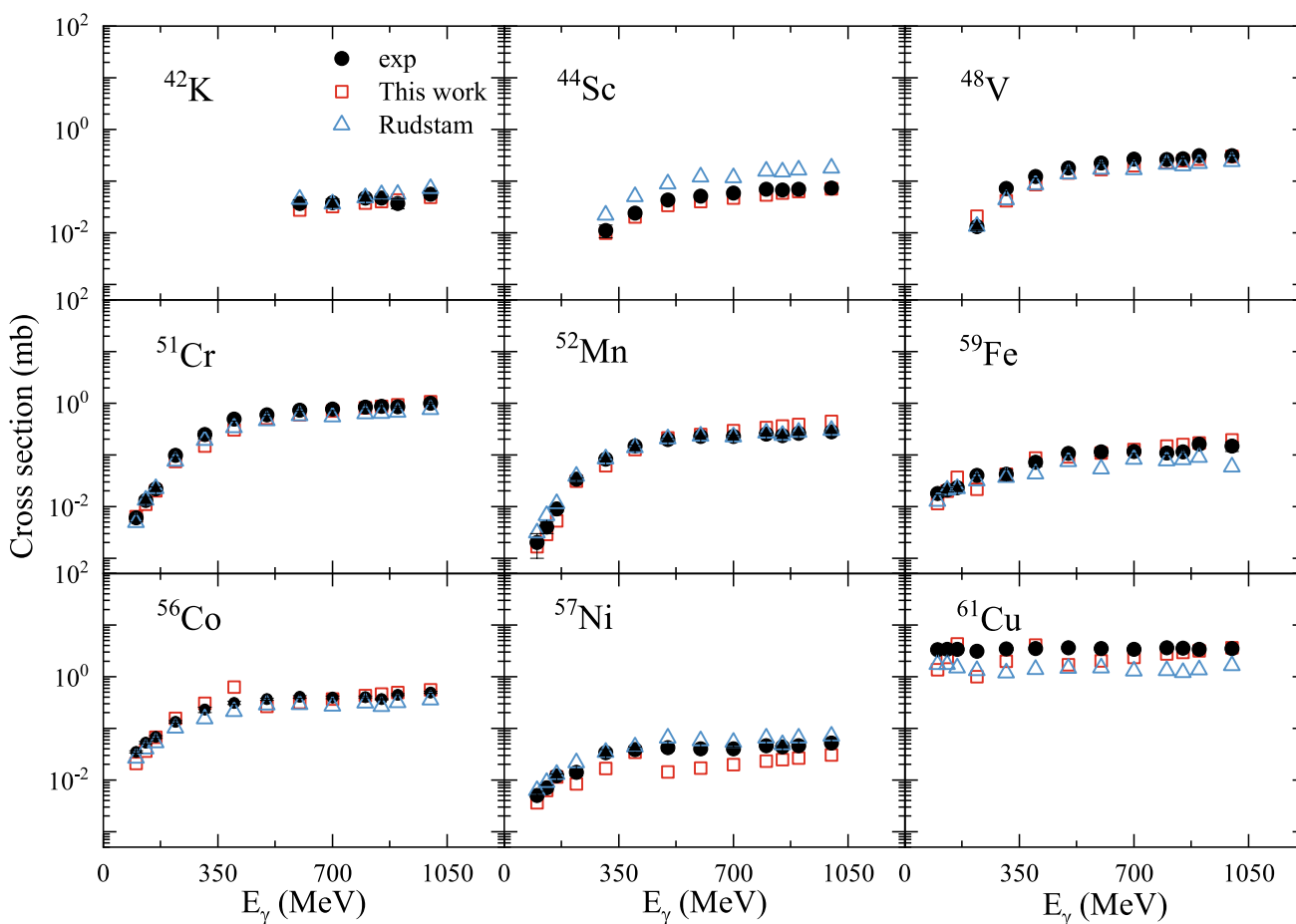


Fig. 4 (Color online) Excitation functions for fragments ^{42}K , ^{44}Sc , ^{48}V , ^{51}Cr , ^{52}Mn , ^{59}Fe , ^{56}Co , ^{57}Ni , and ^{61}Cu produced in reactions of $\gamma+^{64}\text{Cu}$ with E_γ from 100 MeV to 1 GeV. The measured data in

$\gamma+^{\text{nat}}\text{Cu}$ reactions (solid circles) are taken from [4]. The predictions by SPAGINS and the fitting data of the Rudstam formula are plotted in open squares and open triangles, respectively

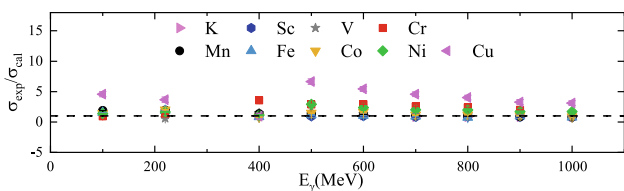
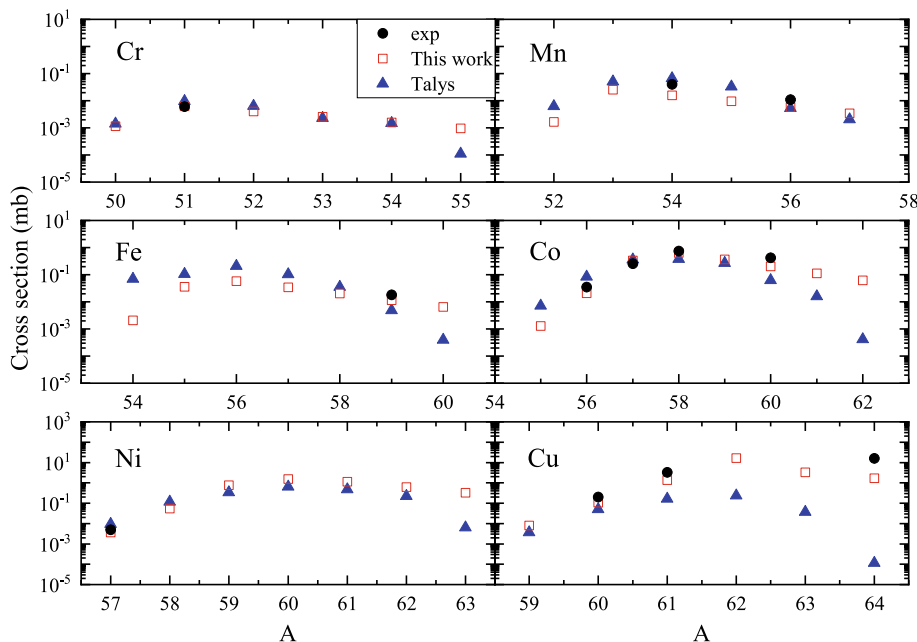


Fig. 5 (Color online) Mean relative error of $^{42,43}\text{K}$, $^{44,46-48}\text{Sc}$, ^{48}V , $^{49,51}\text{Cr}$, $^{52,54,56}\text{Mn}$, ^{59}Fe , $^{56-58,60}\text{Co}$, ^{57}Ni , and $^{60,61,64}\text{Cu}$ produced in the reactions of $\gamma+^{64}\text{Cu}$ for which the incident energies E_γ ranged from 100 MeV to 1 GeV. The dashed line denotes that $\sigma_{exp}/\sigma_{cal}$ is 1

To further verify the SPAGINS formulas, the predicted cross-sections for fragments using the TALYS toolkit and SPAGINS formulas in the 100 MeV $\gamma+^{64}\text{Cu}$ reaction are compared in Fig. 6. The mean relative error between the predictions of the SPAGINS formula and experimental value in the 200 and 900 MeV $\gamma+^{59}\text{Co}$ reactions [52] is shown in Fig. 7. In general, the data predicted by both TALYS and SPAGINS are consistent with the measured data, except for the neutron-rich fragments, in which TALYS predicts relatively lower data. If this phenomenon is valid for neutron-rich fragments, then the SPAGINS predictions agree with the measured data in PNSR. Based on comparisons between the SPAGINS, Rudstam formula, and TALYS toolkits, the SPAGINS formulas provided reasonable predictions for fragments produced in PNSR.

Fig. 6 (Color online) Production cross-sections for Cr, Mn, Fe, Co, Ni, and Cu isotopes in the 100 MeV $\gamma+^{64}\text{Cu}$ reaction. The measured data for $\gamma+\text{natCu}$ reactions (solid circles) are taken from Ref. [4]. The predicted results by the TALYS model and SPAGINS formulas are in open triangles and open squares, respectively



4 Summary

Considering the lack of an effective model to predict the fragments produced in PNSR for high-energy γ -rays, semiempirical formulas named SPAGINS have been proposed, which are suitable for PNSR within the range of $100 \text{ MeV} \leq E_\gamma \leq 1 \text{ GeV}$. The following procedure was followed to construct the SPAGINS formulas: (1) TALYS-1.96 was adopted to find the similarity of fragment production in photon- and proton-induced spallation reactions with the same mass and charge numbers, that is, $\gamma+^{63}\text{Cu}$ and $p+^{62}\text{Ni}$ at 100 and 200 MeV. In this step, the isotopic cross-sectional distributions of the different elements had similar shapes but different magnitudes. This enabled the borrowing of the main concepts of the models for proton-induced spallation reactions. (2) The isotopic cross-sectional distribution of chromium in $\gamma+^{64}\text{Cu}$ at E_γ from 100 MeV to 1 GeV fitted from the Rudstam formula was used to parameterize the incident energy dependence of mass yields in PNSR reactions. (3) Based on steps (1) and (2), the SPAGINS formulas were constructed based on the SPACS formulas for light-charged-particle-induced nuclear spallation reactions, as well as EPAX formulas for projectile fragmentation reactions, by implanting proper modifications to describe fragment distributions. The main characteristics of the excitation function of the mass yield were also established in this step. (4) The predictions of isotopic cross-sections by SPAGINS formulas were compared to the measured data and Rudstam formula, which were in good agreement. The excitation curves of the fragments also support the conclusion that the SPAGINS formulas can predict the fragment cross-section at different E_γ values from 100 MeV to 1 GeV.

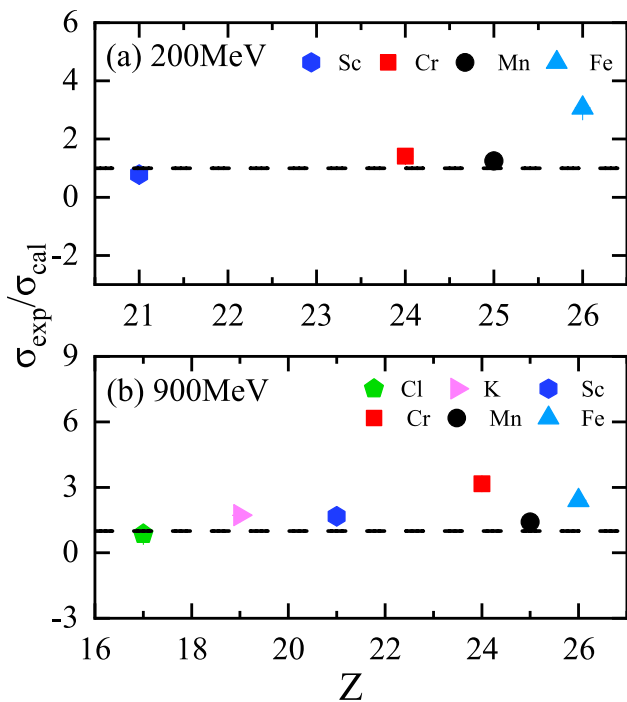


Fig. 7 (Color online) Mean relative error of $^{34,38,39}\text{Cl}$, $^{42,43}\text{K}$, $^{44,46\sim 48}\text{Sc}$, $^{48\sim 51}\text{Cr}$, $^{52,54,56}\text{Mn}$, and $^{52,53}\text{Fe}$ produced in the 200 MeV and 900 MeV γ - ^{59}Co reactions. The measured data are taken from [52]. The dashed line means that $\sigma_{\text{exp}}/\sigma_{\text{cal}}$ is 1

Compared to the Rudstam formula, the SPAGINS formulas overcome this limitation because the parameters are determined from a series of measured data and restricted to limited reaction systems. Meanwhile, the SPAGINS formulas also expand the applicable range of the incident energy compared with the TALYS model (lower than 200 MeV) to 100–1000 MeV. The success of SPACS and EPAX formulas in describing fragment distributions makes the SPAGINS formulas yield reasonable fragment cross-sections, and the fragment excitation curves are suitable for PNSR from E_γ from 100 MeV to 1 GeV. Currently, SPAGINS calculations range from Fe to Zn targets, with charge numbers between 26 and 30 and mass numbers between 58 and 68, which cover common metallic materials in nuclear industrial applications. Considering the rapid development of high-energy γ -ray facilities, SPAGINS formulas provide an effective method for estimating fragment production, γ -nuclear activation, and radiation protection.

Appendix I: SPAGINS formulas

Many SPACS and EPAX formulas are incorporated into the SPAGINS formulas. Owing to the definition of the individual parameters in the formula, SPAGINS adopts gamma

quanta as the target. To present the SPAGINS formula more clearly, detailed formulas are provided in this section.

For a fragment with mass and charge numbers (A, Z), the production cross-section in PNSR is

$$\sigma(A, Z) = \sigma_R Y(A) Y(Z_{\text{prob}} - Z) |_A. \tag{11}$$

For the first term, the reaction cross-section is

$$\sigma_R = 10\pi r_0^2 \left(A_{\text{proj}}^{\frac{1}{3}} + A_{\text{tar}}^{\frac{1}{3}} + \delta_E \right)^2 (1 - B/E_{\text{cm}}) \chi_m, \tag{12}$$

where $r_0 = 1.1$ fm, and

$$B = 1.44 Z_{\text{proj}} Z_{\text{tar}} / H, \tag{13}$$

$$E_{\text{cm}} = E_{\text{proj}} A_{\text{proj}} / (A_{\text{proj}} + A_{\text{tar}}), \tag{14}$$

$$H = r_{\text{proj}} + r_{\text{tar}} + 1.2 \left(A_{\text{proj}}^{\frac{1}{3}} + A_{\text{tar}}^{\frac{1}{3}} \right) / E_{\text{cm}}^{\frac{1}{3}}. \tag{15}$$

One can determine $r_{\text{proj}} = 1.29 r_{\text{proj}}^{\text{rms}}$, and

$$r_{\text{proj}}^{\text{rms}} = 0.891 A_{\text{proj}}^{\frac{1}{3}} \left(1 + 5.565 A_{\text{proj}}^{-\frac{2}{3}} - 1.04 A_{\text{proj}}^{-\frac{4}{3}} \right), r_{\text{tar}}^{\text{rms}} = 0.85.$$

$$\delta_E = 1.85S + \left(0.16S / E_{\text{cm}}^{\frac{1}{3}} \right) - C_E, \tag{16}$$

where

$$S = A_{\text{tar}}^{\frac{1}{3}} A_{\text{proj}}^{\frac{1}{3}} / \left(A_{\text{tar}}^{\frac{1}{3}} + A_{\text{proj}}^{\frac{1}{3}} \right), \tag{17}$$

and

$$C_E = 2.05 [1 - \exp(-E_{\text{proj}}/40) - 0.292 \exp(-E_{\text{proj}}/792) \cos(0.229 E_{\text{proj}}^{0.453})] \tag{18}$$

For $A_{\text{proj}} < 200$,

$$\chi_m = 1 - \chi_1 \exp[-E_{\text{proj}} / (\chi_1 s_1)], \tag{19}$$

in which,

$$\chi_1 = 2.83 - 3.1 \times 10^{-2} A_{\text{proj}} + 1.7 \times 10^{-4} A_{\text{proj}}^2, \tag{20}$$

and

$$s_1 = 0.6, \quad \text{for } A_{\text{proj}} < 12, \tag{21}$$

$$s_1 = 1.6, \quad \text{for } A_{\text{proj}} = 12, \tag{22}$$

$$s_1 = 1.0, \quad \text{for } A_{\text{proj}} > 12. \tag{23}$$

For the second term, the mass distribution considers the contributions from the central ($Y(A)_{\text{cent}}$) and peripheral collisions ($Y(A)_{\text{prph}}$),

$$Y(A) = Y(A)_{\text{cent}} + Y(A)_{\text{prph}}. \tag{24}$$

When considering the incident energy dependence of the mass yield,

$$Y'(A) = G \cdot Y(A) \tag{25}$$

where G is sorted into the following three regions:

$$G = \begin{cases} 10^{(E_\gamma - 100)/100}, & 100 \leq E_\gamma < 220; \\ 10^{(E_\gamma - 220)/300}, & 220 \leq E_\gamma < 500; \\ 10^{(E_\gamma - 500)/2000}, & 500 \leq E_\gamma \leq 1000. \end{cases} \tag{26}$$

The contribution of central collisions to a specific fragment cross-section is

$$Y(A)_{\text{cent}} = (A_{\text{length}} / \{1 + \exp[(A_{\text{proj}} - A'_{\text{cent}} - A) / A_{\text{cent-fluct}}]\}) / A'_{\text{cent}}, \tag{27}$$

where

$$\begin{aligned} A_{\text{cent}} &= \alpha_{\text{cent}} / \exp(A_{\text{proj}} / \beta_{\text{cent}}), \\ A'_{\text{cent}} &= A_{\text{proj}} \{1 - \exp[-\ln(A_{\text{cent}})(E_{\text{proj}}/1000)^{\epsilon_{\text{cent}}}] \}, \\ A_{\text{length}} &= 1, \\ A_{\text{cent-fluct}} &= a_{\text{fluct}} A_{\text{cent}}^{\delta_{\text{fluct}}} (E_{\text{proj}}/1000)^{\epsilon_{\text{cent}}}, \\ a_{\text{fluct}} &= \alpha_{\text{fluct}} + \beta_{\text{fluct}} A_{\text{proj}}. \end{aligned}$$

The contribution of peripheral collisions to a specific fragment cross-section is

$$Y(A)_{\text{periph}} = A_{\text{periph}} \exp\{[A - (A_{\text{proj}} - A_{\text{diff}})] / A_{\text{diff}}\} \times (E_{\text{proj}}/1000)^{\beta_{\text{periph}}} / A'_{\text{cent}}, \tag{28}$$

where

$$\begin{aligned} A_{\text{periph}} &= \alpha_{\text{periph}} + \beta_{\text{periph}} A_{\text{proj}} \\ A_{\text{diff}} &= \alpha_{\text{diff}} + \beta_{\text{diff}} A_{\text{proj}} \end{aligned}$$

The third term $\sigma(A, Z)$ is parameterized by the number of neutron- and proton-rich fragments. For neutron-rich ones,

$$Y(Z_{\text{prob}} - Z)|_A = n f_n \exp(-R|Z_{\text{prob}} - Z|^{u_n}), \tag{29}$$

and proton-rich

$$Y(Z_{\text{prob}} - Z)|_A = n f_p \exp(-R|Z_{\text{prob}} - Z|^{u_p}). \tag{30}$$

Z_{prob} and Z_β take the form of

$$Z_{\text{prob}} = Z_\beta + \Delta_m^{\text{n,p}} + 0.002A + \Delta', \tag{31}$$

$$Z_\beta = \frac{A}{1.98 + 0.0155A^{2/3}}. \tag{32}$$

For a neutron-rich projectile,

$$\begin{aligned} \Delta_m^{\text{n}} &= \{n_1(A/A_{\text{proj}})^6 + n_2[(A_{\text{proj}} - A)/A_{\text{proj}}]\}^2 \\ &\times (Z_{\text{proj}} - Z_{\beta\text{p}}), \end{aligned} \tag{33}$$

For proton-rich projectiles,

$$\Delta_m^{\text{p}} = [\exp(p_1 + p_2 A/A_{\text{proj}})](Z_{\text{proj}} - Z_{\beta\text{p}}), \tag{34}$$

in which $\Delta = \Delta_5 A^2$, $\Delta' = \Delta[1 + d_1(A/A_{\text{proj}} - d_2)^2]$, $n = \sqrt{R/\pi}$, and $R = R_0^{\text{n,p}} R^{\text{phy}}$.

For neutron-rich spallation targets,

$$R_0^{\text{n}} = r_0 \exp[r_3(Z_{\text{proj}} - Z_{\beta\text{p}})], \tag{35}$$

For a proton-rich spallation target,

$$R_0^{\text{p}} = r_0 \exp[r_4(Z_{\text{proj}} - Z_{\beta\text{p}})]. \tag{36}$$

One also has,

$$R^{\text{phy}} = \exp\{-\ln[R_1(A/t_2)]\}. \tag{37}$$

For neutron-rich fragments,

$$U^{\text{n}} = U_{\text{n1}} + U_{\text{n2}} A/A_{\text{proj}}, \tag{38}$$

and proton-rich fragments.

$$U^{\text{p}} = U_{\text{p1}} + U_{\text{p2}} A_{\text{proj}}. \tag{39}$$

The brute force factors f_n presented in Sect. 6.

Appendix II: brute force factor

The ‘‘brute force factor’’ in Eqs. (9) and (10) was parameterized according to the incident energy of the reaction and different ranges of fragment charge numbers. For the energy range of $100 \text{ MeV} \leq E_\gamma < 220 \text{ MeV}$, when $Z \leq 26$,

$$\begin{aligned} f_p &= \frac{1}{10^{(dF/dZ)(Z-Z_{\text{exp}})}} \times 10^{[-12+0.5(Z-1)]} \\ &\times 10^{[0.5(29-Z_{\text{proj}})][5.575-0.175Z]}, \end{aligned} \tag{40}$$

$$\begin{aligned} f_n &= 10^4 \times 10^{[-23+(Z-1)]} \\ &\times 10^{[0.5(29-Z_{\text{proj}})][4.7-0.1Z]} \end{aligned}$$

where

$$\begin{aligned} dF/dZ &= 1.2 + 0.647(A/2)^{0.3}, \\ Z_{\text{exp}} &= Z_{\text{prob}} + dF/dZ \ln(10)/(2R); \end{aligned} \tag{41}$$

when $Z > 26$,

$$\begin{aligned} f_p &= \frac{1}{10^{(dF/dZ)(Z-Z_{\text{exp}})}} \times 10^{[-24+(Z-1)]}, \\ f_n &= 10^4 \times 10^{[-22.5+(Z-1)]}. \end{aligned} \quad (42)$$

For the incident energy range of $220 \text{ MeV} \leq E_\gamma < 500 \text{ MeV}$, when the charge of the fragments $Z \leq 21$,

$$\begin{aligned} f_p &= \frac{1}{10^{(dF/dZ)(Z-Z_{\text{exp}})}} \times 10^{[5.5-0.3(Z-1)]}, \\ f_n &= 10^4 \times 10^{[-15.5+0.75(Z-1)]}, \end{aligned} \quad (43)$$

when $21 < Z \leq 26$,

$$\begin{aligned} f_p &= \frac{1}{10^{(dF/dZ)(Z-Z_{\text{exp}})}} \times 10^{[-8.2+0.4(Z-1)]}, \\ f_n &= 10^4 \times 10^{[-12.6+0.6(Z-1)]}, \end{aligned} \quad (44)$$

when $Z > 26$,

$$\begin{aligned} f_p &= \frac{1}{10^{(dF/dZ)(Z-Z_{\text{exp}})}} \times 10^{[-10+0.5(Z-1)]}, \\ f_n &= 10^4 \times 10^{[-27.7+1.2(Z-1)]}, \end{aligned} \quad (45)$$

For the incident energy range of $500 \text{ MeV} \leq E_\gamma \leq 1000 \text{ MeV}$, when $Z \leq 21$,

$$\begin{aligned} f_p &= \frac{1}{10^{(dF/dZ)(Z-Z_{\text{exp}})}} \times 10^{[5.7-0.3(Z-1)]} \\ &\quad \times 10^{[0.5(29-Z_{\text{proj}})][2.2-0.1Z]}, \\ f_n &= 10^4 \times 10^{[-19.6+0.6(Z-1)]} \\ &\quad \times 10^{[0.5(29-Z_{\text{proj}})][1.15-0.05Z]}, \end{aligned} \quad (46)$$

when $21 < Z \leq 26$,

$$\begin{aligned} f_p &= \frac{1}{10^{(dF/dZ)(Z-Z_{\text{exp}})}} \times 10^{[-7.4+0.4(Z-1)]} \\ &\quad \times 10^{[0.5(29-Z_{\text{proj}})][-2+0.1Z]}, \\ f_n &= 10^4 \times 10^{[-9.5+0.5(Z-1)]} \\ &\quad \times 10^{[0.5(29-Z_{\text{proj}})][-1.9+0.1Z]}, \end{aligned} \quad (47)$$

and when $Z > 26$,

$$\begin{aligned} f_p &= \frac{1}{10^{(dF/dZ)(Z-Z_{\text{exp}})}} \times 10^{[-9.8+0.5(Z-1)]}, \\ f_n &= 10^4 \times 10^{[-14.2+0.7(Z-1)]}. \end{aligned} \quad (48)$$

where parameters from Eqs. (3) to (48) can be found in Refs. [46, 47].

Author Contributions All authors contributed to the study conception and design. Material preparation, data collection, and analysis were performed by Hui-Ling Wei, Pu Jiao, Yu-Ting Wang, Jie Pu, Kai-Xuan Cheng, Ya-Fei Guo, Chun-Yuan Qiao, Gong-Tao Fan, Hong-Wei Wang, and Chun-Wang Ma. The first draft of the manuscript was written by Meng-Die Zhou, and all authors commented on the previous versions of the manuscript. All authors read and approved the final manuscript.

Data Availability Statement The data that support the findings of this study are openly available in Science Data Bank at <https://doi.org/10.57760/sciencedb.j00186.00319> and <https://cstr.cn/31253.11.sciencedb.j00186.00319>.

Declarations

Conflict of Interest Chun-Wang Ma is an editorial board member for Nuclear Science and Techniques and was not involved in the editorial review or the decision to publish this article. All authors declare that there are no competing interests.

References

1. C.W. Ma, Y.G. Ma, Shannon information entropy in heavy-ion collisions. *Prog. Part. Nucl. Phys.* **99**, 120 (2018). <https://doi.org/10.1016/j.pnpnp.2018.01.002>
2. Q. Liu, Q. Normahmedov, M. Jing et al., Determination of cross-sections of natPb(p, x)207Bi and natPb(p, x) 194Hg by GeTHU. *Nuclear Techniques* **46**, 090501 (2023). <https://doi.org/10.11889/j.0253-3219.2023.hjs.46.090501>
3. L. Liu, S. Niu, J. Zhu et al., Motion characteristics and laws of the debris from a near-space nuclear detonation. *Nuclear Techniques (in Chinese)* **45**, 100503 (2022). <https://doi.org/10.11889/j.0253-3219.2022.hjs.45.100503>
4. S. Shibata, M. Imamura, T. Miyachi et al., Photonuclear spallation reactions in Cu. *Phys. Rev. C* **35**, 254 (1987). <https://doi.org/10.1103/PhysRevC.35.254>
5. K. Strauch, Recent studies of photonuclear reactions. *Annu. Rev. Nucl. Sci.* **2**, 105 (1953). <https://doi.org/10.1146/annurev.ns.02.120153.000541>
6. J.S. Levinger, Theories of photonuclear reactions. *Annu. Rev. Nucl. Sci.* **4**, 1 (1954). <https://doi.org/10.1146/annurev.ns.04.120154.000305>
7. F.R. Metzger, Resonance fluorescence in nuclei. *Prog. Nucl. Phys.* **7**, 53 (1959)
8. M. Danos, E.G. Fuller, Photonuclear reactions. *Annu. Rev. Nucl. Sci.* **15**, 29 (1965). <https://doi.org/10.1146/annurev.ns.15.120165.000333>
9. U.E. Berg, U. Kneissl, Recent progress on nuclear magnetic dipole excitations. *Annu. Rev. Nucl. Part. Sci.* **37**, 33 (1987). <https://doi.org/10.1146/annurev.ns.37.120187.000341>
10. U. Kneissl, H.H. Pitz, A. Zilges, Investigation of nuclear structure by resonance fluorescence scattering. *Prog. Part. Nucl. Phys.* **37**, 349 (1996). [https://doi.org/10.1016/0146-6410\(96\)00055-5](https://doi.org/10.1016/0146-6410(96)00055-5)
11. H.R. Weller, M.W. Ahmed, H. Gao et al., Research opportunities at the upgraded HIGS facility. *Prog. Part. Nucl. Phys.* **62**, 257 (2009). <https://doi.org/10.1016/j.pnpnp.2008.07.001>
12. A. Zilges, D.L. Balabanski, J. Isaak et al., Photonuclear reactions-From basic research to applications. *Prog. Part. Nucl. Phys.* **122**, 103903 (2022). <https://doi.org/10.1016/j.pnpnp.2021.103903>
13. R.H. Milburn, Electron scattering by an intense polarized photon field. *Phys. Rev. Lett.* **10**, 75 (1963). <https://doi.org/10.1103/PhysRevLett.10.75>
14. F.R. Arutyunian, V.A. Tumanian, The Compton effect on relativistic electrons and the possibility of obtaining high energy beams. *Phys. Lett.* **4**, 176 (1963)
15. C. Bemporad, R.H. Milburn, N. Tanaka et al., High-energy photons from Compton scattering of light on 6.0-GeV electrons. *Phys. Rev.* **138**, 1546 (1965). <https://doi.org/10.1103/PhysRev.138.B1546>
16. H.W. Wang, G.T. Fan, L.X. Liu et al., Development and prospect of shanghai laser Compton scattering gamma source. *Nucl. Phys.*

- Rev. **37**, 53 (2020). <https://doi.org/10.11804/NuclPhysRev.37.2019043>
17. H.W. Wang, G.T. Fan, L.X. Liu et al., Commissioning of laser electron gamma beamline SLEGS at SSRF. Nucl. Sci. Tech. **33**, 87 (2022). <https://doi.org/10.1007/s41365-022-01076-0>
 18. Y.W. Gong, M. Zhang, W.J. Fan et al., Beam performance of the SHINE dechirper. Nucl. Sci. Tech. **32**, 29 (2021). <https://doi.org/10.1007/s41365-021-00860-8>
 19. N.S. Huang, Z.P. Liu, B.J. Deng et al., The MING proposal at SHINE: megahertz cavity enhanced X-ray generation. Nucl. Sci. Tech. **34**, 6 (2023). <https://doi.org/10.1007/s41365-022-01151-6>
 20. S. Amano, K. Horikawa, K. Ishihara et al., Several-MeV gamma-ray generation at NewSUBARU by laser Compton backscattering. Nucl. Instrum. Methods Phys. Res. Sect. A **602**, 337 (2009). <https://doi.org/10.1016/j.nima.2009.01.010>
 21. D. Habs, T. Tajima, V. Zamfir, Extreme light infrastructure-nuclear physics (ELI-NP): new horizons for photon physics in Europe. Nuclear Phys. News **21**, 23 (2011). <https://doi.org/10.1080/10619127.2010.529741>
 22. A. Deppman, G.S. Karapetyan et al., Bremsstrahlung-induced fission and spallation of the pre-actinide nucleus ^{181}Ta . Phys. Rev. C **91**, 024620 (2015). <https://doi.org/10.1103/PhysRevC.91.024620>
 23. B. Mei, D.L. Balabanski et al., Empirical parametrization for production cross sections of neutron-rich nuclei by photofission of ^{238}U at low energies. Phys. Rev. C **96**, 064610 (2017). <https://doi.org/10.1103/PhysRevC.96.064610>
 24. Guan-Lin. Wang, Hao-Yang. Lan et al., A general framework for describing photofission observables of actinides at an average excitation energy below 30 MeV. Chin. Phys. C **46**, 084102 (2022). <https://doi.org/10.1088/1674-1137/ac6abc>
 25. G. Andersson, I. Blomqvist, B. Forkman et al., Photon-induced nuclear reactions above 1 GeV: (I). Experimental. Nucl. Phys. A **197**, 44 (1972). [https://doi.org/10.1016/0375-9474\(72\)90744-0](https://doi.org/10.1016/0375-9474(72)90744-0)
 26. G.G. Jonsson, K. Lindgren, Photon-induced nuclear reactions above 1 GeV: (I). Experimental. Phys. Scr. **7**, 49 (1973). <https://doi.org/10.1088/0031-8949/7/1-2/004>
 27. K. Lindgren, G.G. Jonsson, Photon-induced nuclear reactions above 1 GeV: (II). Spallation reactions. Nucl. Phys. A **197**, 71 (1972). [https://doi.org/10.1016/0375-9474\(72\)90745-2](https://doi.org/10.1016/0375-9474(72)90745-2)
 28. G.G. Jonsson, B. Persson, High-energy photon induced spallation reactions in ^{127}I . Nucl. Phys. A **153**, 32 (1970). [https://doi.org/10.1016/0375-9474\(70\)90755-4](https://doi.org/10.1016/0375-9474(70)90755-4)
 29. R. Serber, Nuclear reactions at high energies. Phys. Rev. **72**, 1114 (1947). <https://doi.org/10.1103/PhysRev.72.1114>
 30. B. Bülow, B. Johnsson, M. Nilsson et al., Photospallation of ^{51}V at intermediate energies. Zeitschrift für Physik A **278**, 89 (1976). <https://doi.org/10.1007/BF01547346>
 31. G. Rudstam, The evaporation step in spallation reactions. Nucl. Phys. A **126**, 401 (1969). [https://doi.org/10.1016/0375-9474\(69\)90475-8](https://doi.org/10.1016/0375-9474(69)90475-8)
 32. M. Areskoug, B. Schröder, K. Lindgren, Photofission in bismuth at intermediate energy. Nucl. Phys. A **251**, 418 (1975). [https://doi.org/10.1016/0375-9474\(75\)90538-2](https://doi.org/10.1016/0375-9474(75)90538-2)
 33. A. Koning, S. Hilaire, S. Goriely, User Manual of TALYS-1.96 (2021). <https://doi.org/10.1051/ndata:07767>
 34. O.S. Deiev, I.S. Timchenko, S.M. Olejnik et al., Cross-sections of photonuclear reactions $^{65}\text{Cu}(\gamma, n)^{64}\text{Cu}$ and $^{63}\text{Cu}(\gamma, xn)^{63,2s}\text{Cu}$ in the energy range $E_{\gamma \text{ max}} = 35\text{--}94$ MeV. Chin. Phys. C **46**, 124001 (2022). <https://doi.org/10.1088/1674-1137/ac878a>
 35. G.G. Jonsson, K. Lindgren, A complementary study of photospallation systematics. Phys. Scr. **15**, 308 (1977). <https://doi.org/10.1088/0031-8949/15/5-6/004>
 36. G.G. Jonsson, K. Lindgren, Pion effects in $^{127}\text{I}(\gamma, xn)$ reactions of high multiplicity. Nucl. Phys. A **141**, 355 (1970). [https://doi.org/10.1016/0375-9474\(70\)90851-1](https://doi.org/10.1016/0375-9474(70)90851-1)
 37. A.J. Koning, S. Hilaire, M.C. Duijvestijn, TALYS-1.0, ND 2007—International Conference on Nuclear Data for Science and Technology, April 22–27, Nice, France. ND2007:058 (2007). <https://doi.org/10.1051/ndata:07767>
 38. A.J. Koning, J.P. Delaroche, Local and global nucleon optical models from 1 keV to 200 MeV. Nucl. Phys. A **713**, 231 (2003). [https://doi.org/10.1016/S0375-9474\(02\)01321-0](https://doi.org/10.1016/S0375-9474(02)01321-0)
 39. D.G. Madland, Meeting on the nucleon-nucleus optical model up to 200 MeV. Bruyeres-le-Chatel, France, November 13–15 (1996). [arXiv:nucl-th/9702048](https://arxiv.org/abs/nucl-th/9702048)
 40. A. Koning, S. Hilarie, S. Goriely, Manual for TALYS 1.96, pp. 75–80
 41. G. Rudstam, Systematics of spallation yields. Zeitschrift für Naturforschung A **21**, 1027 (1966). <https://doi.org/10.1515/zna-1966-0724>
 42. S.G. Rudstam, XLII. Spallation of elements in the mass range 51–75. Philos. Mag. J. Sci. **46**, 344 (1955). <https://doi.org/10.1080/14786440308521088>
 43. R. Silberberg, C.H. Tsao, Partial cross-sections in high-energy nuclear reactions, and astrophysical applications I targets with $z \leq 28$. APJ Suppl. Ser. **25**, 315 (1973). <https://doi.org/10.1086/190271>
 44. K. Sümmerer, B. Blank, Modified empirical parametrization of fragmentation cross sections. Phys. Rev. C **61**, 034607 (2000). <https://doi.org/10.1103/PhysRevC.61.034607>
 45. K. Sümmerer, Improved empirical parametrization of fragmentation cross sections. Phys. Rev. C **86**, 014601 (2012). <https://doi.org/10.1103/PhysRevC.86.014601>
 46. C. Schmitt, K.-H. Schmidt, A. Kelić-Heil, SPACS: a semi-empirical parameterization for isotopic spallation cross sections. Phys. Rev. C **90**, 064605 (2014). <https://doi.org/10.1103/PhysRevC.90.064605>
 47. C. Schmitt, K.-H. Schmidt, A. Kelić-Heil, Erratum: SPACS: a semi-empirical parameterization for isotopic spallation cross sections [Phys. Rev. C 90, 064605 (2014)]. Phys. Rev. C **94**, 039901 (2016). <https://link.aps.org/doi/10.1103/PhysRevC.94.039901>
 48. K. Sümmerer, W. Brühle, D.J. Morrissey et al., Target fragmentation of Au and Th by 2.6 GeV protons. Phys. Rev. C **42**, 2546 (1990). <https://doi.org/10.1103/PhysRevC.42.2546>
 49. K. Sümmerer, Erratum: Improved empirical parametrization of fragmentation cross sections [Phys. Rev. C 86, 014601 (2012)]. Phys. Rev. C **87**, 039903 (2013). <https://link.aps.org/doi/10.1103/PhysRevC.87.039903>
 50. R.K. Tripathi, F.A. Cucinotta, J.W. Wilson, Accurate universal parameterization of absorption cross sections. Nucl. Instrum. Methods Phys. Res. Sect. B **117**, 347 (1996). [https://doi.org/10.1016/0168-583X\(96\)00331-X](https://doi.org/10.1016/0168-583X(96)00331-X)
 51. R.K. Tripathi, J.W. Wilson, F.A. Cucinotta, Accurate universal parameterization of absorption cross sections II—neutron absorption cross sections. Nucl. Instrum. Methods Phys. Res. Sect. B **129**, 11 (1997). [https://doi.org/10.1016/S0168-583X\(97\)00121-3](https://doi.org/10.1016/S0168-583X(97)00121-3)
 52. S.R. Sarkar, M. Soto, Y. Kubota, Photospallation of complex nuclei at intermediate energies. I. Radiochimica Acta **55**, 113 (1991). <https://doi.org/10.1524/ract.1991.55.3.113>

Springer Nature or its licensor (e.g. a society or other partner) holds exclusive rights to this article under a publishing agreement with the author(s) or other rightsholder(s); author self-archiving of the accepted manuscript version of this article is solely governed by the terms of such publishing agreement and applicable law.